Fluid Dynamics &
Materials Processing

Tech Science Press

http://doi.org/10.32604/fdmp.2026.079847

ARTICLE

Numerical Investigation of Flow and Heat Transfer in a Spider-Web-Inspired Microchannel Heat Sink

Liang Yin[1,*], Youjia Gao[2], Jie Ding[1] and Sichao Su[1]

[1]College of Mechanical Engineering, Hunan University of Arts and Science, Changde, China
[2]Hunan Gaochuang Xiangyu Technology Co., Ltd., Changde, China
*Corresponding Author: Liang Yin. Email: yl88222@126.com

Received: 29 January 2026; Accepted: 08 April 2026; Published: 07 May 2026

ABSTRACT: To address the thermal management challenges associated with localized high heat flux in electronic chips, this study proposes a bionic spider-web microchannel heat sink using deionized water as the coolant. Numerical simulations are conducted for two configurations, one with pinfins at the hotspot (Model A) and one without pinfins (Model B). The effects of Reynolds number and hotspot heat flux on flow distribution, pumping power, thermal resistance and temperature uniformity are systematically analyzed. Results show that the flow distribution varies significantly among channels, with higher flow rates near the inlet. Increasing the Reynolds number raises pumping power but reduces thermal resistance and improves hotspot temperature uniformity. Varying the heat flux variation has little effect on pumping power and thermal resistance; nevertheless, higher heat flux values lead to an increases in the temperature difference across the hotspot, worsening uniformity. The pinfin structure enhances local heat transfer, strengthens hotspot cooling and improves overall temperature uniformity. It is shown that a spider-web heat sink can effectively manage a heat flux as high as 480 W/cm^2, thereby demonstrating its potential for next-generation high-power electronics cooling.

KEYWORDS: Bionic; spiderweb structure; pump power; thermal resistance; temperature uniformity; microchannel heat sink; hotspot cooling

1 Introduction

As electronic components continue to advance through miniaturization and integration, their internal architectures are growing increasingly intricate. While this evolution drives a steady enhancement in operational efficiency, it simultaneously induces a sharp rise in chip-level heat flux—often culminating in localized high-temperature hotspots. Such excessive thermal accumulation poses a serious threat to both the performance and service life of electronic devices, thereby intensifying the challenges associated with effective thermal management [1–4]. For contemporary microprocessors, the average heat flux reaches approximately 100 W/cm^2, with hotspot regions exceeding 1000 W/cm^2 [5–7]. This highly concentrated thermal load triggers an exponential increase in both local junction temperature and temperature gradient, significantly diminishing the device's mean time between failures (MTBF). Consequently, chip reliability and operational stability deteriorate, ultimately shortening its functional lifespan.

In recent years, a growing number of sophisticated microchannel heat sink configurations have been proposed. Inspired by biological systems, researchers have increasingly adopted biomimetic principles to guide the structural optimization and topological design of conventional microchannel

heat sinks—leveraging naturally evolved structures renowned for their exceptional thermal and fluidic performance. Widely explored biomimetic geometries include tree-like, T-shaped, honeycomb, and wavy configurations, among others. Table 1 summarizes representative biomimetic structures alongside their key findings.

Table 1: Bionic structures and key performance characteristics.

	Author(s)	Bionic Structure	Main Results	Reference
1	Krishna	Leaf vein	(a) Absorption time reduced by 73% (b) Peak temperature lowered by 12.88 K (c) Saturation time decreased by 88%	[8]
2	Balakrishnan	shark skin	(a) Heat transfer coefficient enhanced by 15% (b) Thermal resistance reduced to 0.17°C/W (c) Junction temperature lowered by 50°C	[9]
3	Han	petal-type	(a) temperature reduced by 21.81 K (b) efficiency increased by 1.26 times (c) PEC enhanced by 1.5 times	[10]
4	Dastan	spider web	(a) Fiber deposition rate increased from 35% to 90% (b) Pressure drop validated with 8.5% deviation (c) Flow division deviation within ±2.7%	[11]
5	Corcione	honeycomb	(a) Heat transfer enhancement reached up to 116% (b) Peak enhancement achieved with 5 × 5 honeycomb (c) Critical Rayleigh number increased with cell count	[12]
6	Hu	ant nest	(a) the pressure drop is reduced by 51% (b) the temperature is reduced by 60%	[13]
7	Wang	dragonfly wing	(a) the maximum temperature is 14.3 K lower than SRM (smooth rectangular microchannel) (b) the heat transfer efficiency is 218 percent higher than SRM	[14]
8	Wang	cicada wing	(a) the condensation heat transfer (CHT) efficiency is increased by 320%	[15]
9	Chen	branching vessel tree system	(a) stronger heat transfer capability (b) lower pumping power	[16]

The bionic fractal microchannel heat sink was optimized using an artificial neural network (ANN) coupled with response surface methodology (RSM). The optimal geometric and operational parameters were determined to be t/b = 0.2, h/b = 0.2, and Re = 1000, yielding an efficiency index of 1.07 and a prediction accuracy of 99.9%. A reduction in the thermal conductivity of the constituent material led to a deterioration in thermal performance [17]. To address the thermal management challenges associated with high-power electronic components, Li et al. [18] developed a snowflake-inspired fractal biomimetic microchannel heat sink-featuring variable-width primary channels and integrated secondary flow channels. Comparative analysis demonstrates that the proposed configuration (Structure II) achieves markedly enhanced thermal performance relative to the baseline fractal design (Structure I), yielding an approximately 14.4% increase in the Nusselt number. Concurrently, it substantially reduces hydraulic resistance, as evidenced by a 12.65% reduction in pressure drop. Moreover, the incorporation of nanofluids further improves heat transfer performance. The fractal-inspired microchannel heat sink was optimized using gradient-based, direct-search, and genetic algorithms [19]. The resulting optimal geometries minimize either pressure drop or flow power while satisfying practical fabrication constraints. Higher heat fluxes tend to favor configurations with fewer branching levels and a greater number of inlet channels. Notably, simplified

geometry-based designs achieve thermal–hydraulic performance within 13% of that attained by the fully optimized configurations. Wang et al. [20] developed a BTMS incorporating a bionic "runner" structure inspired by the geometric features of natural spider webs. They comprehensively examined the effects of key runner structural parameters—as well as inlet velocity—on the overall thermal performance of the system. Their findings indicated that the bionic spider web channel structure effectively reduces power consumption in electronic water pumps, achieving over 60% lower pressure drop compared to honeycomb structures. A sharkskin-inspired main-side rib microchannel heat sink was designed. The influences of side-rib height, valley width, and side-rib inclination angle on thermal-hydraulic performance were systematically investigated [21]. Results demonstrate that the proposed design effectively reduces entropy generation and enhances key thermal performance metrics-by up to a factor of 1.071–2.241-while increasing the side-rib-to-main-rib height ratio is found to be beneficial for heat transfer enhancement.

These findings not only confirm that diverse bionic structures can substantially enhance the heat transfer performance of microchannels but also establish a critical reference and foundational basis for enriching and advancing bionic microchannel heat transfer technology systems. Despite extensive research on bionic structures for thermal management, systematic investigations into the flow and heat transfer characteristics of spider-web-inspired microchannel heat sinks-particularly under localized hotspot conditions-remain scarce. Specifically, the impact of pin-fin integration on flow distribution uniformity and hotspot temperature regulation has yet to be thoroughly explored. To address this gap, this study proposes two configurations of spider-web microchannel heat sinks: one integrated with pin-fins (Model A) and one without (Model B). Their thermal–hydraulic performance is comprehensively evaluated via numerical simulation across a range of Reynolds numbers and heat fluxes. The novelty of this work lies in its systematic comparative analysis of key performance metrics-including flow distribution uniformity, thermal resistance, pumping power, and temperature uniformity-as well as its experimental and numerical demonstration of effective ultra-high heat flux dissipation up to 480 W/cm^2. Collectively, the results offer actionable design guidelines for high-efficiency thermal management solutions tailored to next-generation electronic devices.

2 Model

2.1 Problem Description

The microchannel heat sink investigated in this study is designed to dissipate heat generated by high-power electronic chips during operation. The chip is mounted directly atop the heat sink's cooling surface, while the interior of the heat sink features a microchannel cavity with varying topological configurations. A cooling fluid enters through the inlet and flows through the microchannels to extract thermal energy from the chip located on the upper surface. Fig. 1a illustrates the fundamental geometry of the spider-web-inspired microchannel design. The corresponding schematic diagrams for the spider-web microchannel are presented in Fig. 1a–c, with all geometric parameters tabulated in Table 2. Two distinct configurations are examined: Model A incorporates pin fins localized at the hotspot region (Fig. 1b), whereas Model B omits pin fins entirely.

Table 2: Design parameters of the spider web microchannel.

Spider Web Microchannel (μm)								
Microchannel Dimension						Hotspot Dimension		
H_c	H_h	W_r	W_c	L_b	α	H_b	H_p	L_p
50	70	30	30	1000	3°	10	40	30

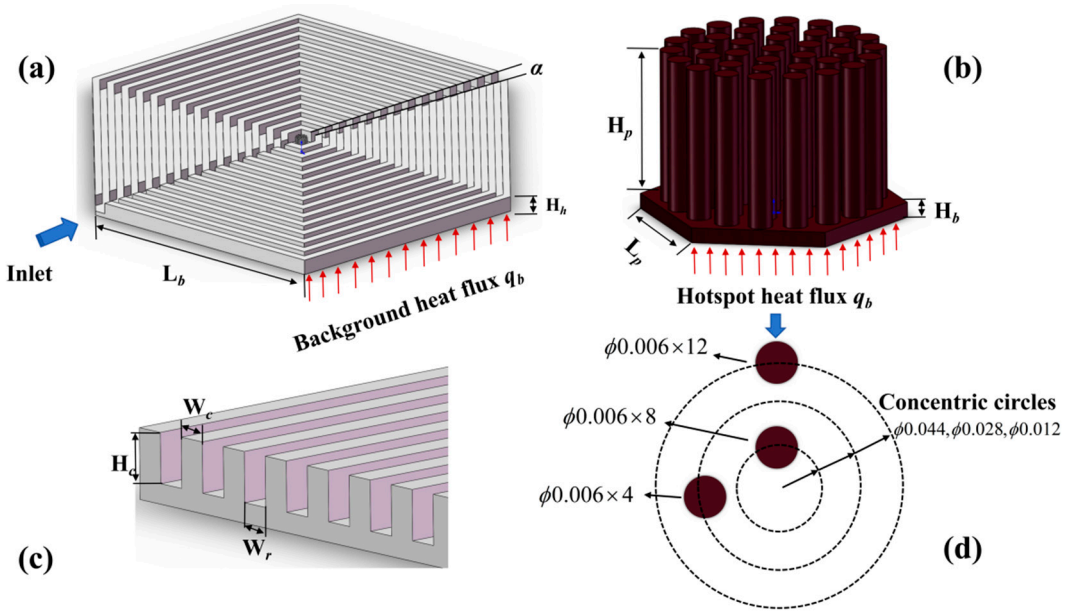

Figure 1: Diagrams of the spider web microchannel heat sink: (**a**) Microchannel heat sink with pinfin (model A), (**b**) pinfin of the heat sink, (**c**) geometric of the microchannel, (**d**) arrangement of pinfin.

2.2 Numerical Method

In this paper, we employ a fluid-solid coupling numerical simulation method alongside Fluent 2022 software to analyze the heat sink of spider web micro-channels. To simplify the calculations, the following assumptions are made:

(1) The flow is assumed to be laminar due to the low velocity of the fluid.
(2) The influences of body forces, viscous dissipation, and compressibility are disregarded.
(3) Velocity slip and temperature jump at the fluid-solid coupling interface are not taken into account.

The mass conservation equation for the fluid region is listed as follow [22]:

$$\nabla \cdot (\rho_f \vec{V}) = 0 \tag{1}$$

The momentum conservation equations for the fluid region are listed as follow:

$$\vec{V} \cdot \nabla(\rho_f \vec{V}) = -\nabla p + \nabla \cdot (\mu_f \nabla \vec{V}) \tag{2}$$

The energy conservation equation for the fluid region is listed as follow:

$$\vec{V} \cdot \nabla(\rho_f c_{pf} T_f) = \nabla \cdot (\lambda_f \nabla T_f) \tag{3}$$

In the solid domain, the thermal conduction equation is numerically solved.

$$\nabla \cdot (\lambda_s \nabla T_s) = 0 \tag{4}$$

2.3 Boundary Condition

The velocity inlet boundary condition is applied at the channel entrance, with the inlet velocity varied from 3.2 m/s to 19.2 m/s, corresponding to Reynolds numbers ranging from 200 to 1200. A pressure outlet

boundary condition is imposed at the exit, with a fixed back pressure of 0.1 MPa. The background heat flux is maintained at 40 W/cm^2. Based on literature findings [7], the hotspot heat flux is set to six times the background value; to systematically investigate the thermal performance limits of the model, the hotspot heat flux is further varied over the range of 160–480 W/cm^2.

In this study, all physical parameters are defined as piecewise functions. Silicon is selected as the solid-phase material owing to its compatibility with standard microfabrication processes widely employed in electronic chip integration. Although silicon exhibits lower thermal conductivity than copper or aluminum, it offers superior mechanical stability and minimizes thermal expansion mismatch with typical semiconductor chip substrates. Deionized water is adopted as the coolant, given its favorable thermophysical properties, chemical inertness toward silicon, and extensive use in microchannel cooling applications [23]. The solid domain is modeled using silicon, with a specific heat capacity C_s = 712 J/Kg·K, density ρ_s = 2330 kg/m^3, and thermal conductivity governed by Eq. (5).

$$k_s = 75 \times \left(\frac{T}{300}\right)^{-0.32} \exp(-5.3 \times 10^{-4} \times (T - 300)) \tag{5}$$

The coolant selected for this study is water, which exhibits thermo-physical properties that are dependent on temperature. The corresponding relationships are presented in Eqs. (6)–(9) [23].

$$\begin{aligned} c_{p,f}(T) = {} & 4217 - 3.452 \times T_f + 1.155 \times 10^{-1} T_f^2 - 1.862 \times 10^{-3} T_f^3 \\ & + 1.538 \times 10^{-5} T_f^4 - 4.850 \times 10^{-8} T_f^5 \end{aligned} \tag{6}$$

$$\begin{aligned} \rho_{p,f}(T) = {} & 999.9 + 9.561 \times 10^{-2} T_f - 1.013 \times 10^{-2} T_f^2 + 8.459 \times 10^{-5} T_f^3 \\ & - 3.496 \times 10^{-7} T_f^4 \end{aligned} \tag{7}$$

$$\begin{aligned} k_f = {} & 5.698 \times 10^{-1} + 1.772 \times 10^{-3} T_f - 4.870 \times 10^{-6} T_f^2 - 2.915 \times 10^{-8} T_f^3 \\ & + 1.094 \times 10^{-10} T_f^4 \end{aligned} \tag{8}$$

$$\begin{aligned} \mu_f(T) = {} & 1.750 \times 10^{-3} - 5.558 \times 10^{-5} T_f + 1.172 \times 10^{-6} T_f^2 - 1.579 \times 10^{-8} T_f^3 \\ & + 1.169 \times 10^{-10} T_f^4 - 3.535 \times 10^{-13} T_f^5 \end{aligned} \tag{9}$$

$c_{p,f}$ is the specific heat capacity of the fluid, $\rho_{p,f}$ is the density of the fluid, k_f is the specific heat of the fluid, and μ_f represents the viscosity coefficient of the fluid.

2.4 Description of Performance Parameters

The Reynolds number (Re) is defined as:

$$\mathrm{Re} = \frac{\rho_f u D_h}{\mu_f} \tag{10}$$

ρ_f is the fluid density (water), and μ_f is the dynamic viscosity. The Reynolds number is calculated at the inlet of a channel.

The hydraulic diameter of a channel is defined as:

$$D_h = \frac{4A}{P} = \frac{2(W_c H_c)}{W_c + H_c} \tag{11}$$

The performance of the heat sink is assessed based on three key parameters: maximum thermal resistance, pumping power, and overall performance factor. The maximum thermal resistance is defined as follows [14]:

$$R_{th,\max} = \frac{T_{\max,h} - T_{in}}{Q_{\text{avg}}(A_b + A_h)} \tag{12}$$

where Q_{avg} is the average heat flux applied at the base of the microchannel, which is calculated by:

$$Q_{\text{avg}} = \frac{q_b A_b + q_h A_h}{A_b + A_h} \tag{13}$$

where the subscript b stands for the background and h stands for the hotspot.

The pumping power is defined as:

$$P_{pump} = A_c \times U_{in} \times \Delta P \tag{14}$$

Temperature uniformity Φ was used as a parameter to evaluate heat sink heat transfer uniformity [24]:

$$\varphi = \frac{T_{ave}}{T_{\max}} \tag{15}$$

where the $T_{\max}$ is the maximum temperature of hotspot and the T_{ave} is the meam temperature of hotspot.

2.5 Grid Independence Analysis

To enhance computational efficiency while maintaining numerical accuracy, a tetrahedral structured mesh was employed for model pre-processing, as illustrated in Fig. 2. The first layer height was set to 1 μm with a stretching ratio of 1.2 to ensure adequate resolution of near-wall gradients. In addition, boundary layer meshing was applied on the fluid side of the solid–liquid interface to improve the resolution of flow characteristics adjacent to the interface. To strike a balance between computational accuracy and resource utilization, grid independence of the computational domain was verified.

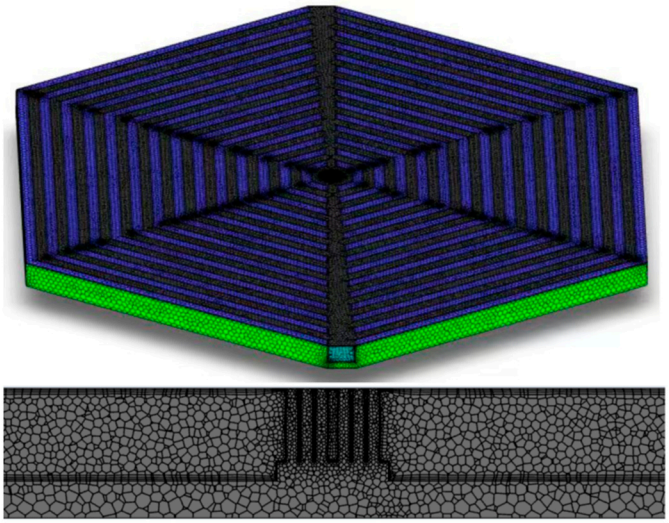

Figure 2: Global grid and sectional local grid.

At a Reynolds number (Re) of 1200, the heat fluxes at the hotspot and background regions were 40 W/cm^2 and 480 W/cm^2, respectively. The thermal resistance and maximum temperature were evaluated for four mesh configurations: 743,650; 1,079,487; 1,607,106; and 2,812,865 cells. As summarized in Table 3, when the cell count increased from approximately 1.08 million to 1.61 million, the deviations in heat sink thermal resistance and maximum temperature were only 0.062% and 1.53%, respectively. Accordingly, a mesh configuration of around 1.6 million cells was selected for the present study, as it provides sufficient resolution for computational accuracy while optimizing resource utilization.

Table 3: Grid independence validation.

	Cells	Nodes	T_{max}	Diference%	R_t	Diference%
Mesh1	743,650	2,601,629	308.03	0.358%	1.154	3.78%
Mesh2	1,079,487	3,943,505	307.49	0.182%	1.147	3.15%
Mesh3	1,607,106	6,111,929	307.12	0.062%	1.129	1.53%
Mesh4	2,812,865	11,634,757	306.93	-	1.112	-

3 Results and Discussions

3.1 Flow Distribution Characteristic

To investigate the flow distribution characteristics of microchannel heat sink structures, the flow distribution coefficient m_i/m was introduced for analysis. These characteristics play a critical role in determining the overall temperature distribution within such structures. In practical operation, the heat sink is cooled in a parallel configuration; however, flow variations inevitably arise among the cooling branches due to the sub-confluence nature of the channels and the location of the coolant inlet. Therefore, a comprehensive analysis of the flow distribution behavior in microchannel heat sink structures is essential.

Fig. 3 illustrates the effects of Reynolds number and heat flux on the flow distribution characteristics for two distinct designs, Model A and Model B. It can be observed that the flow distribution among the individual channels exhibits significant variation, which is attributed to the diverging configuration of the spider-web-like structure. In general, the flow tends to concentrate near the inlet region, with the flow rate in each channel gradually decreasing from channel 1 to channel 13. As the Reynolds number increases from 200 to 1200, the flow rate in the main channel shows a progressive increase.

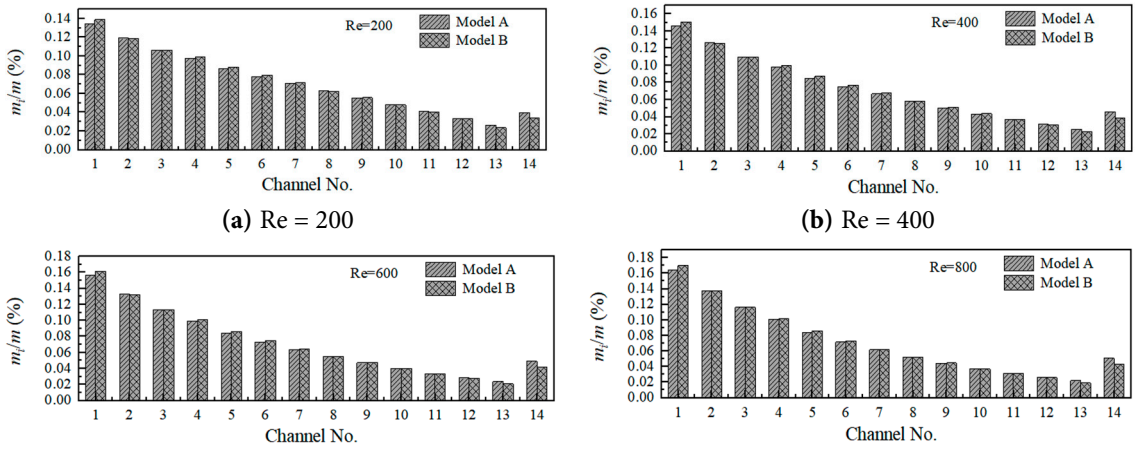

(a) Re = 200

(b) Re = 400

(c) Re = 600

(d) Re = 800

Figure 3: *Cont.*

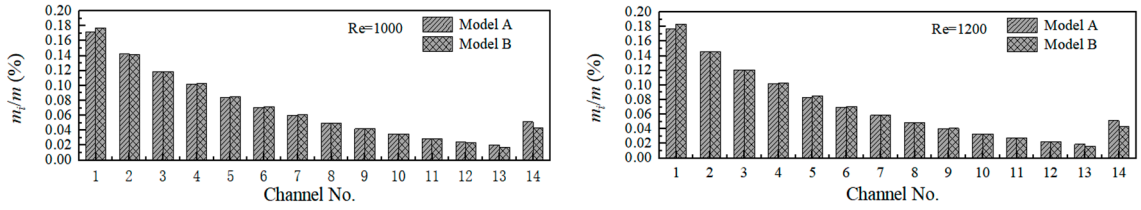

(e) Re = 1000 **(f)** Re = 1200

Figure 3: Effect of Reynolds number on flow distribution characteristics.

As the heat flux increases, the flow distribution coefficient for each individual channel exhibits minimal variation. However, as illustrated in Fig. 4, the overall distribution across all channels follows a consistent trend: the flow rate gradually decreases from channel 1 to channel 13, accompanied by a slight increase in mainstream channel 14. A comparison between Model A and Model B reveals that the differences in flow distribution coefficients among the channels are smaller in Model A, indicating superior flow uniformity. The observed non-uniform distribution is attributed to the radial divergence of the channels and the variation in pressure drop along the flow path. Channels located closer to the inlet experience lower flow resistance, resulting in higher mass flux. As the Reynolds number increases, inertial effects become dominant, promoting a more uniform flow distribution. This effect is particularly pronounced in Model A, where the presence of pin fins introduces local flow resistance that helps balance the distribution.

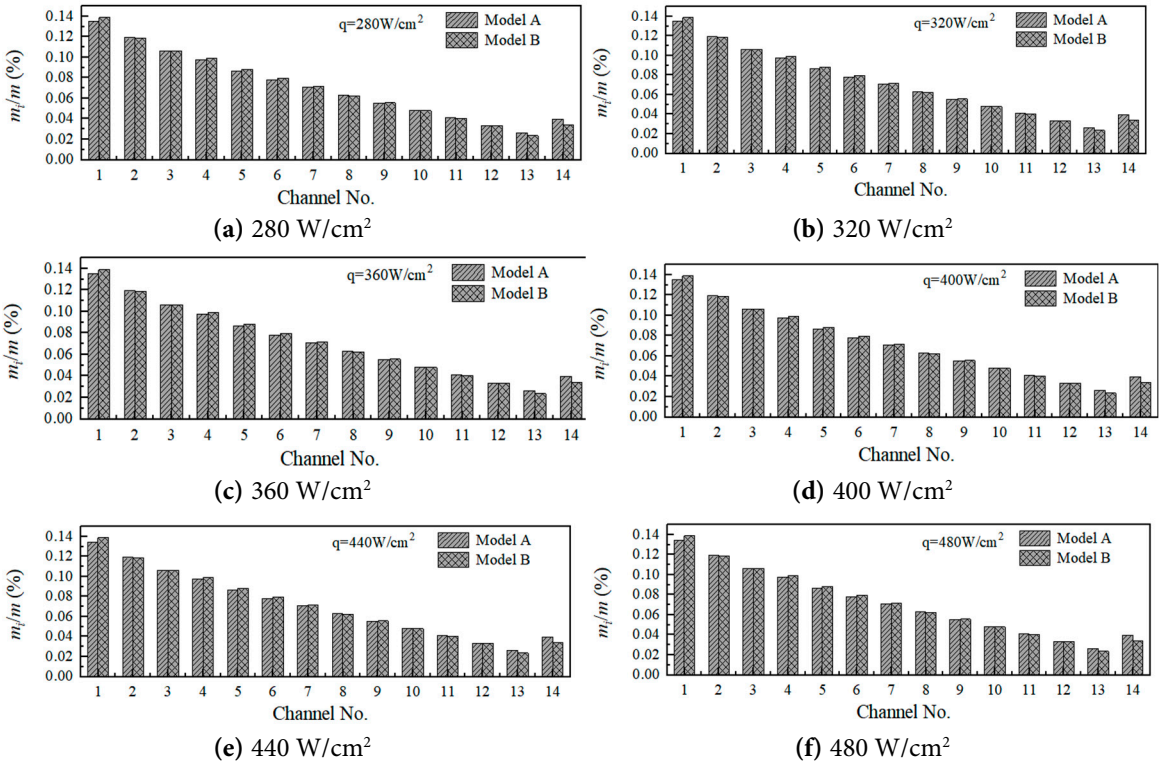

(a) 280 W/cm² **(b)** 320 W/cm²

(c) 360 W/cm² **(d)** 400 W/cm²

(e) 440 W/cm² **(f)** 480 W/cm²

Figure 4: Effect of heat flux on flow distribution characteristics.

3.2 Thermal Performance

To further evaluate the heat dissipation performance of the bionic spider-web structure, this analysis focuses on three key metrics: total pumping power, total thermal resistance, and the temperature uniformity

coefficient at the hotspot. As shown in Fig. 5, the pumping power for both Model A and Model B increase with Reynolds number. This rise is attributed to the increased pressure drop resulting from higher flow rates, which in turn demands greater pumping power. At Re = 800, the pumping powers for Model A and Model B are 0.0151 m·W and 0.0113 m·W, respectively, reflecting a difference of approximately 25%. This indicates that the integration of pin fins in Model A introduces additional disturbances to the fluid flow, thereby elevating the pumping power requirement. In addition, thermal resistance is observed to decrease with increasing Reynolds number. However, the difference in thermal resistance between the two models remains relatively small, with Model B exhibiting slightly higher values than Model A.

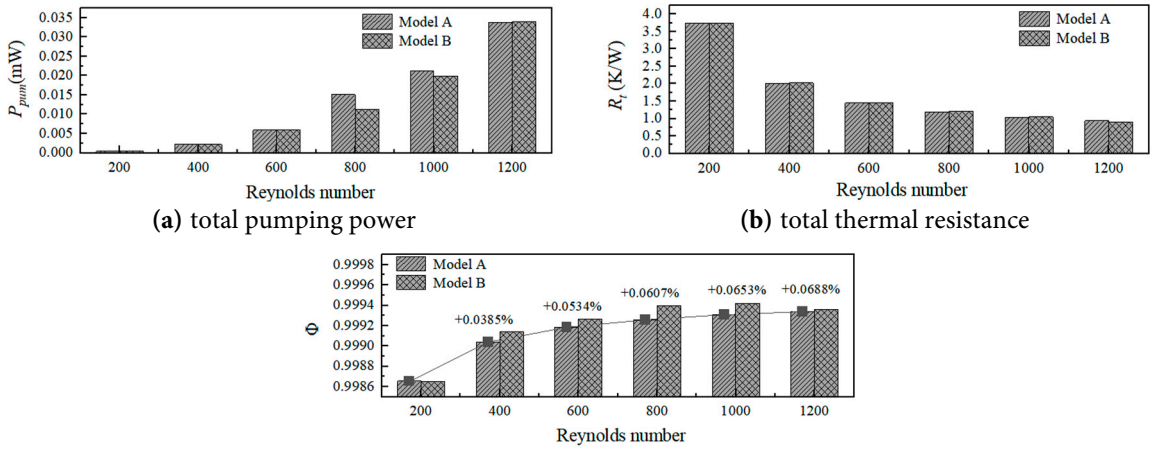

(a) total pumping power **(b)** total thermal resistance

(c) temperature uniformity coefficient

Figure 5: Thermal performance of modes A and B varies with the Reynolds number.

This study also examines the uniformity of temperature distribution at the hotspot, as illustrated in Fig. 5c. The results indicate that higher Reynolds numbers lead to improved temperature uniformity. Specifically, as the Reynolds number increases from 200 to 1200, the temperature uniformity coefficient of Model A rises from 0.0385% at Re = 400 to 0.0688% at Re = 1200. These findings suggest that elevated local flow velocities enhance heat transfer, thereby strengthening hotspot cooling and contributing to more uniform temperature distribution across the chip surface.

Fig. 6 illustrates the variations in pumping power, thermal resistance, and temperature uniformity coefficient as a function of heat flux. For both Model A and Model B, the pumping power and thermal resistance exhibit only minor variations. As the heat flux increases from 240 to 480 W/cm^2, the pumping power for Model A decreases by approximately 0.0364% and 0.881%, respectively, while the thermal resistance declines by 49.81% and 49.92%. As shown in Fig. 6c, the temperature uniformity coefficient exhibits an inverse dependence on heat flux; specifically, as the heat flux rises from 240 to 480 W/cm^2, the coefficient for Model A decreases from −0.0145% (at q_h = 280 W/cm^2) to 0.0678% (at q_h = 480 W/cm^2).

The temperature contours at the hotspot are presented in Figs. 7 and 8. The incorporation of the pinfin structure at the hotspot does not substantially alter the temperature distribution on its surface; notably, the highest temperature occurs at the coolant inlet. At a Reynolds number (Re) of 200, the difference between the maximum and minimum temperatures for Model A and Model B is approximately 0.84 K and 1.2 K, respectively. When Re increases to 1000, these differences decrease to about 0.588 K and 0.6 K, respectively. This indicates that as the Reynolds number increases, the temperature disparity at the hotspot for both models diminishes, leading to a more uniform temperature distribution.

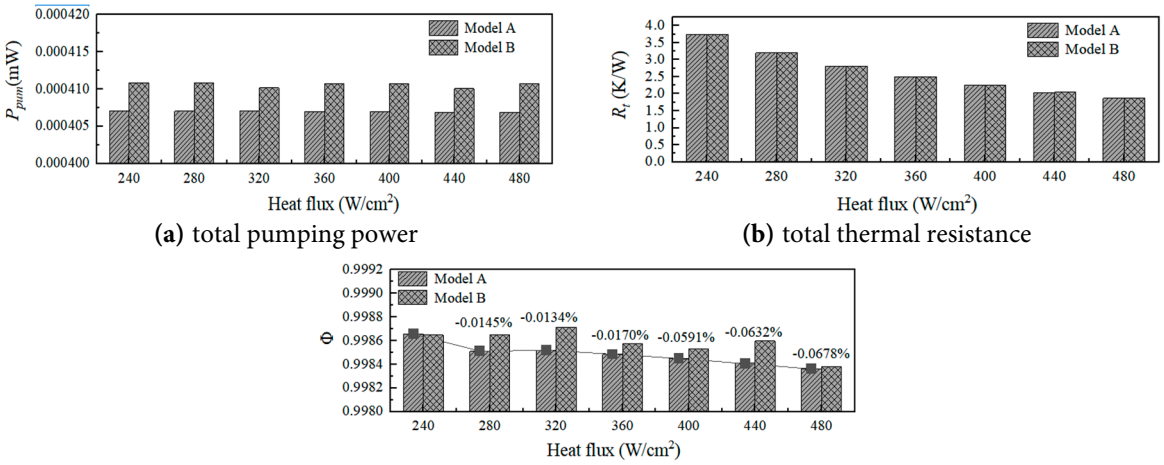

(a) total pumping power **(b)** total thermal resistance

(c) temperature uniformity coefficient

Figure 6: Thermal performance of modes A and B varies with the heat flux.

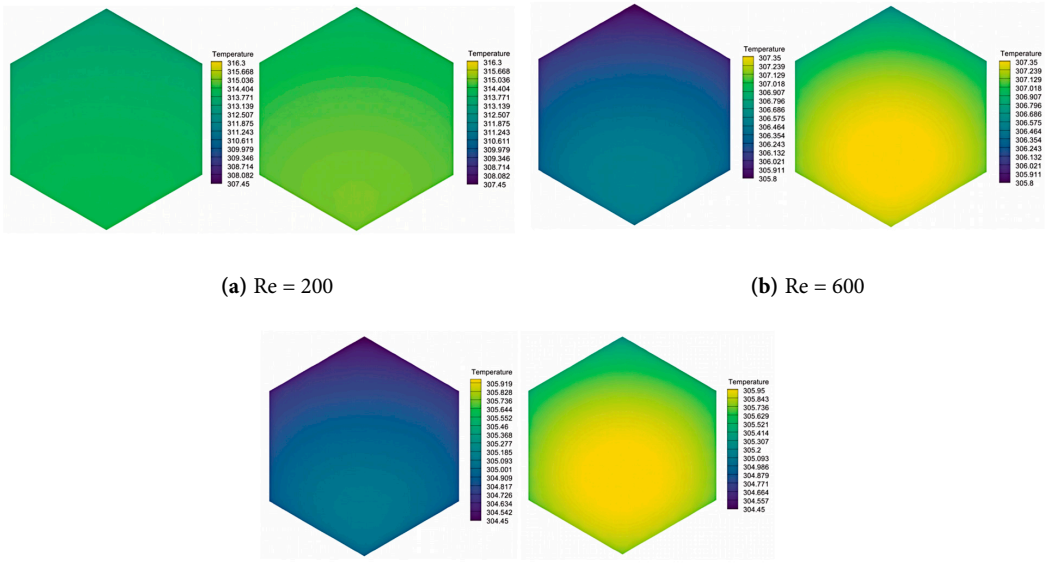

(a) Re = 200 **(b)** Re = 600

(c) Re = 1000

Figure 7: Temperature contours of the hot spots at Re = 200, 600 and 1000 (left: Model A; right: Model B) (unit: K).

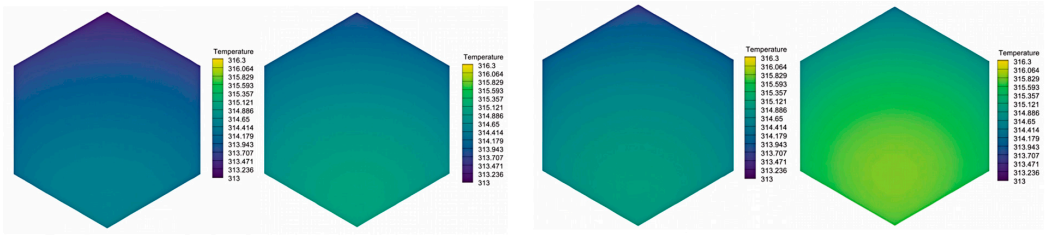

(a) q_h = 280 W/cm^2 **(b)** q_h = 360 W/cm^2

Figure 8: *Cont.*

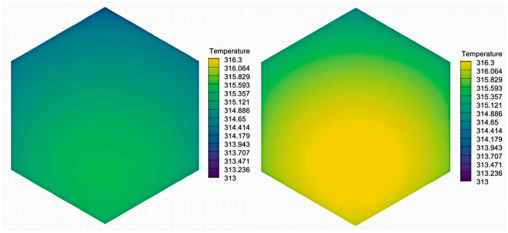

(c) q_h = 440 W/cm^2

Figure 8: Temperature contours of the hot spots at q_h = 280, 360 and 440 W/cm^2 (left: Model A; right: Model B) (unit: K).

4 Conclusions

In this paper, a bionic spider-web microchannel heat sink structure is proposed to address the challenge of hotspot cooling in electronic chips. The effects of key parameters, including Reynolds number and heat flux, on the transient heat transfer performance are analyzed, leading to the following conclusions:

(1) The flow distribution coefficient varies significantly across individual channels, with greater uniformity observed in channels closer to the inlet. A comparison between Model A and Model B indicates that Model A exhibits smaller differences in the flow distribution coefficients among its channels, thereby achieving improved flow distribution uniformity.

(2) Total pumping power increases with rising Reynolds number, whereas thermal resistance decreases accordingly. At Re = 800, the total pumping power for Model A and Model B is 0.0151 m·W and 0.0113 m·W, respectively, representing a difference of approximately 25%. As the Reynolds number increases from 200 to 1200, the temperature uniformity coefficient of Model A rises from 0.0385% (at Re = 400) to 0.0688% (at Re = 1200).

(3) Both total pumping power and thermal resistance exhibit only minor variations with changes in heat flux. As the heat flux increases from 240 W/cm^2 to 480 W/cm^2, the total pumping power for Model A and Model B decreases by approximately 0.0364% and 0.881%, respectively, while the thermal resistance decreases by about 49.81% and 49.92%, respectively. Notably, with increasing heat flux, the disparity between the maximum and minimum temperatures at the hotspot becomes more pronounced, resulting in a less uniform temperature distribution.

(4) The incorporation of a pin-fin structure significantly enhances heat transfer efficiency at the hotspot while promoting greater temperature uniformity across the chip surface. Overall, Model A demonstrates superior performance compared to Model B.

(5) Future work will employ multi-objective optimization algorithms, such as genetic algorithms or surrogate-based optimization, to identify optimal geometric parameters for simultaneously minimizing thermal resistance and pumping power.

Acknowledgement: This research was funded by the Key Project of Hunan Provincial Education Department (Grant No.: 24A0477).

Funding Statement: This research was funded by the Key Project of Hunan Provincial Education Department (Grant No.: 24A0477). The APC was funded by the same project.

Author Contributions: The authors confirm contribution to the paper as follows: Software, Liang Yin and Jie Ding; investigation, Liang Yin, Youjia Gao and Sichao Su; resources, Liang Yin; data curation, Liang Yin and Jie Ding;

writing—original draft preparation, Liang Yin; writing—review and editing, Liang Yina nd Jie Ding; visualization, Liang Yin; supervision, Jie Ding; project administration, Youjia Gao; funding acquisition, Sichao Su. All authors reviewed and approved the final version of the manuscript.

Availability of Data and Materials: The data that support the findings of this study are available from the Corresponding Author, [Liang Yin], upon reasonable request.

Ethics Approval: Not applicable.

Conflicts of Interest: The authors declare no conflicts of interest.

Nomenclature

A	the flow channel area (m^2)
C	the specific heat capacity (J/Kg·K)
H	the flow channel height (m)
L	the flow channel width (m)
P	the pumping power (m·W)
Q	the heat flux (W/m^2)
R	the thermal resistance (K/W)
T	the temperature (K)
α	the expansion angle (°)
λ	the conductivity coefficient (W/(m·K)
ρ	the fluid density (kg/m^3)
Φ	the temperature uniformity coefficient
μ	the dynamic viscosity (kg/(m·s)
Subscript	
avg	the average value
b	the background
c	the channel
f	the fluid
h	the hotspot
max	the maximum value
pum	the pumping
s	the solid

References

1. Baba M, Ishiharajima H, Ishisaka K, Yamada N, Takeda M. Temperature-leveling performance comparison of solid–solid phase change materials for thermal management of electronic chips in thin devices. J Therm Sci Technol. 2024;19(1):24-00014. [CrossRef].
2. Farahikia M, Wang PC, Reyes L, Krumholtz M. A comparative numerical analysis of cold plates for thermal management of chips with hotspots. J Electron Packag. 2024;146(3):034501. [CrossRef].
3. Husain S, Asif M, Khan KA. Comparative analysis of thermal interface materials for effective thermal management of electronic devices. Exp Heat Transf. 2025;38(5):405–24. [CrossRef].
4. Shen J, Chen X, Xu X, Kong J, Song Z, Wang X, et al. Thermal performance of a hybrid cooling plate integrated with microchannels and PCM. Appl Therm Eng. 2024;236:121917. [CrossRef].
5. Darbari B, Kefayati G, Wang XL, Vafai K. Application of micro-channel heat sinks for thermal management of electric vehicle components: A comprehensive review. Energy Convers Manag. 2026;347:120507. [CrossRef].
6. Yin L, Jiaqiang E, Tu Y, Luo W. Biomimetic microchannel structures and their topological optimization: a review. Int Commun Heat Mass Transf. 2025;163:108689. [CrossRef].
7. Ansari D, Kim KY. Hotspot thermal management using a microchannel-pinfin hybrid heat sink. Int J Therm Sci. 2018;134:27–39. [CrossRef].

8. Krishna KV, Pandey V, Maiya MP. Bio-inspired leaf-vein type fins for performance enhancement of metal hydride reactors. Int J Hydrogen Energy. 2022;47(56):23694–709. [CrossRef].
9. Balakrishnan P, Muthuram A. Bioinspired heat transfer and thermal management. In: Biomimetic and bioinspired materials. New York, NY, USA: CRC Press; 2025. p. 144–68. [CrossRef].
10. Han ZJ, Wang J, Liu HL, Shao XD, Ge XB, Qiao JK, et al. Numerical and experimental analysis of a novel bionic petal-type heat exchanger. Int Commun Heat Mass Transf. 2026;172:110369. [CrossRef].
11. Dastan A, Abouali O. Microfiber motion and web formation in a microchannel heat sink: a numerical approach. Comput Fluids. 2013;71:28–40. [CrossRef].
12. Corcione M, Quintino A, Ricci E. Heat transfer enhancement in Rayleigh-Bénard convection of liquids using suspended adiabatic honeycombs. Int J Therm Sci. 2018;127:351–9. [CrossRef].
13. Hu K, Lu C, Yu B, Yang L, Rao Y. Optimization of bionic heat sinks with self-organized structures inspired by termite nest morphologies. Int J Heat Mass Transf. 2023;202:123735. [CrossRef].
14. Wang Z, Li B, Luo QQ, Zhao W. Effect of wall roughness by the bionic structure of dragonfly wing on microfluid flow and heat transfer characteristics. Int J Heat Mass Transf. 2021;173:121201. [CrossRef].
15. Wang R, Zhu J, Meng K, Wang H, Deng T, Gao X, et al. Bio-inspired superhydrophobic closely packed aligned nanoneedle architectures for enhancing condensation heat transfer. Adv Funct Mater. 2018;28(49):1800634. [CrossRef].
16. Chen Y, Cheng P. Heat transfer and pressure drop in fractal tree-like microchannel nets. Int J Heat Mass Transf. 2002;45(13):2643–8. [CrossRef].
17. Vaferi K, Vajdi M, Nekahi S, Heydari A, Sadegh Moghanlou F, Nami H, et al. Thermo-hydraulic performance optimization of a disk-shaped microchannel heat sink applying computational fluid dynamics, artificial neural network, and response surface methodology. Heliyon. 2023;9(10):e21031. [CrossRef].
18. Li W, Qi C, Xue C. Snowflake fractal bionic microchannel heat sink applied for thermal management of electronic components. J Therm Anal Calorim. 2025;150(22):18587–606. [CrossRef].
19. Heymann D, Pence D, Narayanan V. Optimization of fractal-like branching microchannel heat sinks for single-phase flows. Int J Therm Sci. 2010;49(8):1383–93. [CrossRef].
20. Wang J, Liu X, Liu F, Liu Y, Wang F, Yang N. Numerical optimization of the cooling effect of the bionic spider-web channel cold plate on a pouch lithium-ion battery. Case Stud Therm Eng. 2021;26:101124. [CrossRef].
21. Wang R, He G, Li D, Shi Y, Meng Z, Zhang N, et al. Numerical investigation of laminar flow heat transfer characteristics and entropy generation in microchannel with shark-skin bionic structure. Int J Heat Fluid Flow. 2025;116:109954. [CrossRef].
22. Ansari D, Raza W, Jeong JH, Kim KY. A novel hybrid-composite microchannel heat sink for extreme hotspot mitigation. Int J Therm Sci. 2025;208:109473. [CrossRef].
23. Li P, Guo D, Huang X. Heat transfer enhancement, entropy generation and temperature uniformity analyses of shark-skin bionic modified microchannel heat sink. Int J Heat Mass Transf. 2020;146:118846. [CrossRef].
24. Gonzales GV, dos Santos ED, Isoldi LA, Rocha LAO, da Silva Neto AJ, Telles WR. Constructal design of double-T shaped cavity with stochastic methods luus-jaakola and simulated annealing. Defect Diffus Forum. 2017;370:152–61. [CrossRef].